frontiers in Marine Science

TYPE Original Research
PUBLISHED 11 June 2026
DOI 10.3389/fmars.2026.1797236

OPEN ACCESS

EDITED BY
Dongfeng Xie,
Zhejiang Institute of Hydraulics & Estuary, China

REVIEWED BY
Zhixuan Feng,
East China Normal University, China
Philip Pika,
Université libre de Bruxelles, Belgium

*CORRESPONDENCE
Jérôme Chappellaz
jerome.chappellaz@epfl.ch

RECEIVED 27 January 2026
REVISED 21 May 2026
ACCEPTED 28 May 2026
PUBLISHED 11 June 2026

CITATION
Hassler C, Delille B, Lavanchy S, Cruz H, Grilli R, Jaccard S and Chappellaz J (2026) Low methane supersaturation observed in southwestern Greenland fjords.
Front. Mar. Sci. 13:1797236.
doi: 10.3389/fmars.2026.1797236

Low methane supersaturation observed in southwestern Greenland fjords

Christel Hassler[1], Bruno Delille[2], Sébastien Lavanchy[1], Hugo Cruz[1], Roberto Grilli[3], Samuel Jaccard[4] and Jérôme Chappellaz[1]*

[1]Ecole Polytechnique Fédérale de Lausanne, ENAC, Smart Environmental Sensing in Extreme Environments (SENSE), Sion, Switzerland, [2]Chemical Oceanography Unit, FOCUS, University of Liège, Liège, Belgium, [3]University Grenoble Alpes, CNRS, IRD, Grenoble INP, Institut des Géosciences de l'Environnement (IGE), Grenoble, France, [4]Institute of Earth Sciences, University of Lausanne, Lausanne, Switzerland

Climate-driven retreat of Greenland's marine-terminating glaciers in rapidly transforming fjord systems has potential implications for marine methane cycling. Because the Greenland ice sheet and its basal meltwaters have been identified as sources of methane, it has been hypothesized that fjords fed by marine-terminating glaciers should be associated with elevated dissolved methane concentrations and enhanced sea-air exchange. Here, we test this hypothesis by comparing two adjacent fjords in southwest Greenland (Narsaq region), one currently fed by a marine-terminating glacier, and one supplied by a pro-glacial river draining a glacier that has retreated inland. Measurements collected during the summers of 2023 and 2024 reveal remarkably similar dissolved methane concentrations, vertical distributions and saturation levels in both fjords. Methane concentrations were highest in surface meltwaters and fjord waters and lower in intruding oceanic waters into the fjords, with no evidence for significant methane inputs from the seafloor. Overall, the observed methane concentrations (4.94 – 9.30 nM) correspond to a surface layer (0-3m) saturation of 129-226% resulting in small atmospheric fluxes from 0.49 to 3.31 μmol m^{-2} d^{-1}. High-resolution measurements using a membrane inlet laser spectrometer (MILS) further revealed no detectable fine-scale methane enrichment near the glacier front. We attribute the similarity in dissolved methane distributions between the two fjords to the dominance of surface meltwater discharge during summer, even in the presence of a marine-terminating glacier, suggesting that southern Greenland fjords represent a relatively weak source of atmospheric methane under summer conditions. Our results suggest that ongoing retreat from marine-terminating to land-terminating glaciers is unlikely to substantially enhance methane emission from Greenland fjords under present and near-future summer conditions. Wintertime measurements remain needed to fully constrain annual methane budgets in these fjords.

KEYWORDS
arctic, climate change, fjord, glacier, methane

1 Introduction

Methane (CH_4) is a potent greenhouse gas accounting for approximately 20% of the effective radiative forcing attributable to anthropogenic activities (IPCC, 2021). Aquatic systems collectively contribute nearly half of global CH_4 emissions (Rosentreter et al., 2021), yet substantial uncertainties remain regarding the magnitude and controls of emission from specific environments. In particular, rapidly changing systems remain poorly constrained in current methane budgets. There is currently a large imbalance between known CH_4 sources and sinks, indicating that important emissions remain insufficiently quantified. A significant contribution from aquatic systems, particularly from inland waters and human-altered systems, has been proposed as a key factor contributing to discrepancy (Rosentreter et al., 2021; Rocher-Ros et al., 2023). In polar regions, CH_4 release may be further amplified by climate-driven glacier retreat and permafrost thaw, processes that mobilize previously stored carbon and promote CH_4 production and release (Portnov et al., 2016; Lamarche-Gagnon et al., 2019; Kleber et al., 2023). Together, these factors underscore the urgent need for improved mapping and quantification of CH_4 sources in these vulnerable environments.

Outlet glaciers from the Greenland ice sheet discharge substantial volumes of meltwater and sediment, products of intense subglacial erosion, into adjacent fjords (Mankoff et al., 2017; Overeem et al., 2017). This meltwater, enriched in CH_4 produced beneath the ice sheet (Lamarche-Gagnon et al., 2019), is delivered to the fjord systems via subglacial discharge at the grounding line, proglacial rivers, and subsurface drainage pathways (Portnov et al., 2016; Kleber et al., 2023). However, the extent to which these inputs translate into enhanced dissolved methane concentrations and emissions towards the atmosphere at the fjord scale remains poorly constrained. Despite these inputs, observations of dissolved methane in fjords systems remain scarce (Dieser et al., 2014; Christiansen and Jørgensen, 2018; Juncher Jørgensen et al., 2020). Ongoing climate warming is driving the retreat of marine-terminating glaciers (further referred as MTG), with many fjords expected to transition to systems predominantly fed by land-terminating glaciers and proglacial rivers (further referred as LTG).This shift is anticipated to fundamentally alter freshwater delivery pathways, sediment transport and biogeochemical cycling along Arctic coastlines, yet its implications for the regional methane cycle remain poorly constrained. Because subglacial meltwater is a source of methane (Lamarche-Gagnon et al., 2019), we hypothesized higher dissolved CH_4 concentrations in fjords fed by MTG compared to those fed by LTG due to direct inputs of subglacial meltwater at depth, particularly in summer when meltwater discharge peaks (Gräff et al., 2025). This hypothesis predicts increased methane concentrations and potentially increased sea-air fluxes in MTG fjords.

In fjords fed by MTGs, meltwater is discharged at depth beneath the calving front, driving buoyant upwelling of relatively warm and nutrient-rich subsurface waters. This process enhances surface productivity by increasing nutrient input in the euphotic zone (Meire et al., 2017; Wood et al., 2025). In contrast, fjords associated with LTGs lack deep subglacial meltwater inputs, resulting in weaker vertical mixing and less productive waters. These contrasting physical regimes of MTG and LTG fjords may influence methane production, transport and retention. Therefore, if the persistent subsurface CH_4 supersaturation, widely observed in the ocean - the so-called methane paradox - occurs in fjord systems, subsurface methane levels may be higher in MTG fjords due to enhanced biologically-mediated CH_4 production linked to elevated primary productivity. This methane paradox has indeed challenged the long-standing assumption that CH_4 production occurs exclusively under anoxic conditions via archaeal methanogenesis (Mao et al., 2024). While early explanations invoked CH_4 release from sediments or anoxic microenvironments within sinking particles (Repeta et al., 2016; Mao et al., 2022), recent studies revealed multiple oxic pathways for CH_4 production, including bacterial and phytoplankton degradation of nitrogen- and sulfur-rich compounds (Ernst et al., 2022; Mao et al., 2022; Klintzsch et al., 2023), methylphosphonate degradation by cyanobacteria (Perez-Coronel and Beman, 2022), and biotic interactions between cyanobacteria and methanogenic archaea (Ye et al., 2024).

Traditional measurements of dissolved CH_4 rely on discrete water sampling, followed by laboratory analysis, which, while providing high analytical precision, offer limited spatial and temporal resolution and are thus poorly suited for resolving fine-scale variability in dynamic marine environments. Recent advances in sensor technology have substantially improved our ability to detect CH_4 sources including deep seeps, gas hydrates, subglacial meltwater, thawing permafrost, sediment inputs, mid-ocean ridges, and hydrothermal systems (Grilli et al., 2021, 2023; Dolven et al., 2022; Kapit et al., 2024). These sensors are compact and can be deployed on standard oceanographic platforms such as CTD rosettes, moorings, and autonomous underwater vehicles (AUVs) (Kapit et al., 2024). Despite these advances, commercially available sensors (HydroC CH_4, METS, Mini CH_4 Pro) are primarily designed for detecting high-concentration anomalies and dispersion, rather than to resolve background CH_4 distributions or fine-scale vertical structure. Their broad dynamic ranges and slow response times - up to 4800 s (Mini CH_4 specifications) - limit their effectiveness in profiling mode and in physically dynamic environments. They often require complex post-processing or statistical corrections to interpret the data reliably (Dolven et al., 2022). Moreover, detection limits (10–100 nM) are too high to capture background CH_4 levels in marine systems, which typically range from 5–20 nM (Rhee et al., 2009), making them ill-suited for quantitative diagnostics away from major CH_4 sources.

To address these limitations, we deployed a prototype membrane inlet laser spectrometer (MILS), a high-sensitivity, fast-response instrument previously validated under controlled laboratory conditions (Grilli et al., 2018) and successfully applied in freshwater and coastal environments, including polar systems, to detect CH_4 emissions from sedimentary and seepage sources (Jansson et al., 2019; Grilli et al., 2021; 2023; Dolven et al., 2022). MILS offers the fastest response time (8–30 seconds at 25°C) combined with exceptionally low detection limits (below 1 nM), enabling fine-scale vertical profiling of CH_4 distribution in dynamic aquatic environments including background concentrations typical of marine systems (~5–20 nM, Rhee et al., 2009). We deployed MILS in rapidly evolving fjord systems of southwest Greenland

experiencing rapid glacier retreat. Our objective was to compare adjacent fjords fed by MTG and LTG glaciers over 2 consecutive years to assess the relative importance of subglacial and sedimentary CH_4 sources and to quantify for potential outgassing to the atmosphere in these contrasting glacier-fjord systems. More specifically, we hypothesized that MTG fjords would exhibit higher dissolved CH_4 than LTG ones, due to direct subglacial meltwater inputs. All results presented here focus on summer conditions.

2 Methods

2.1 Study region and oceanographic settings

This study focuses on fjord systems in southwest Greenland near Narsaq, a region undergoing rapid warming and pronounced landscape transformation. To illustrate the biogeochemical consequences of glacier retreat, we compared two adjacent fjords with contrasting glacial configurations: Igalikup Kangerlua, fed by a proglacial river draining a LTG (river outlet approximately at 60.907°N, 45.264°W) and Ikersuaq Sermilik, which hosts the marine-terminated glacier (MTG) Eqalorutsit Kangillit Sermiat (EkaS: calving front approximately at 61.32°N, 45.785°W). Given that surrounding North Atlantic waters entering these fjords have low dissolved CH_4 concentrations close to atmospheric equilibrium (Rhee et al., 2009), CH_4 inputs from glacial meltwater or sedimentary sources can be readily detected against this low background of 5–20 nM (Rhee et al., 2009). This research forms part of the interdisciplinary GreenFjord project, which integrates six thematic clusters, Land, Human, Biodiversity, Cryosphere, Atmosphere, and Ocean, to provide a holistic understanding of ecosystem changes and their implications for local communities (https://greenfjord-project.ch/).

For each field campaign, stations were numbered sequentially from fjord head (Stn O1, MTG, Stn L1, LTG) towards the continental shelf, with stations occupied in 2024 identified by the suffix "b". Stations from 2023 (Stn O5, O6, O10, O11, O13; L4, L3, L6, L8, L9) were revisited in 2024 corresponding to Stns O2b, O3b, O8b, O9b, O10b, and O15b; and to Stns L1b, L2b, L3b, L5b, and L6b, respectively (Figure 1; Supplementary Table 1). Oceanographic conditions were characterized using CTD profiles collected across multiple stations. In total, 26 were sampled in 2023 and 18 in 2024 using an Idronaut Ocean Seven 316 Plus CTD, with 5 additional stations sampled in 2024 using the Seabird 911 system (Supplementary Table 1). Both CTDs were equipped with sensors for dissolved oxygen and chlorophyll *a* (Chl *a*) fluorescence. Deployments were conducted aboard *RV Sanna* (22 Aug–4 Sept 2023; 10–22 July 2024) and *RV Forel* (2–9 July 2024). Minor discrepancies in salinity between CTDs (Supplementary Figure 1) were attributed to differing conductivity-to-salinity conversion algorithms. To ensure consistency, salinity was recalculated using the Fofonoff and Millard (1983) formulation employed by the Idronaut system. Fluorescence readings from the Chelsea TriLux (Idronaut) and the ECO FLNTU sensor (Seabird) differed significantly, and no consistent cross-calibration could be established. Consequently, the Chl *a* data from SeaBird deployments at stations O9b and O10b, where Idronaut measurements were not available, were excluded from further analysis.

2.2 MILS sensor

Methane concentration profiles were acquired using the MILS at 11 stations across both fjords in 2023. In 2024, MILS deployments were limited to 5 stations in the MTG fjord due to instrument failure (Supplementary Table 1).

2.2.1 Principle and characteristics

The MILS sensor deployed in this study is a refined version of the SubOcean system originally described by Grilli et al. (2018) and subsequently applied in marine (Grilli et al., 2021; Dolven et al., 2022) and freshwater environments (Grilli et al., 2023). The instrument relies on a patented membrane-based extraction method that enables rapid sampling of dissolved gases (Triest et al., 2017), coupled with an optical spectrometer operating in the mid-infrared (3.3 μm) using optical feedback cavity-enhanced

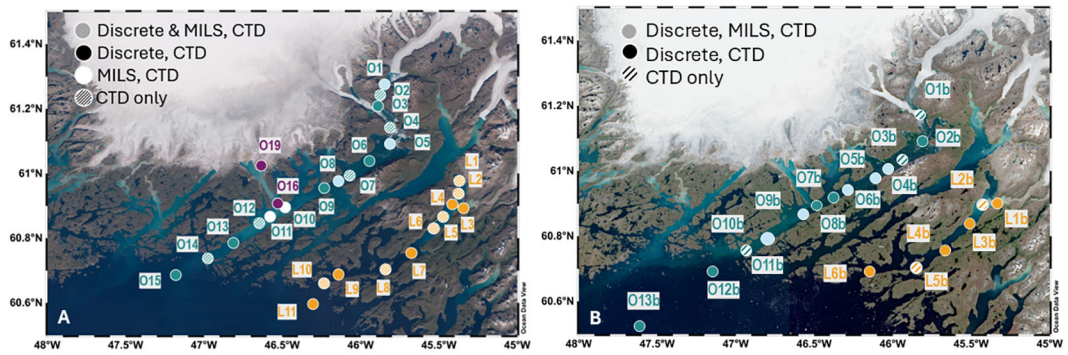

FIGURE 1
Station map overlaid on Copernicus Sentinel-2 satellite map at time of sampling [3rd Sept., 2023, **(A)** 14th July, 2024, stations identified by a "b" letter, **(B)**]. The fjord with the marine-terminating glacier (MTG) is shown in blue whereas the fjord with the land-terminating glacier (LTG) is shown in orange. In 2023 a side fjord in the MTG was also sampled (O16 and O19) and is shown in purple.

absorption spectroscopy (OFCEAS; Morville et al., 2014). A prototype version of this MILS was deployed during the 2023 campaign, while a commercial version manufactured by the French company A2 Photonic Sensors (A2PS) was used in 2024. Prior to and following the field campaign in 2024, the commercial MILS was calibrated against certified standard gases including known CH_4 concentration in air. No significant drift was detected. However, the 2023 prototype could not be recalibrated after the expedition, leading to the flow measurement drift described in Section 3.2. This is the reason why the 2023 MILS data are used here only for qualitative comparison.

The extraction module consists of a 10-µm thick PDMS membrane housed in a stainless-steel casing and flushed with water at a flow rate of 0.8 L min^{-1} using a submersible pump (SBE 5T). Gases permeating the membranes are carried to the spectrometer through flexible PFA tubing. A controlled flow of dry carrier gas (Zero Air) is injected on the lee side of the membrane to enhance gas transfer, and maintain membrane efficiency. Flow regulation is achieved using a pressure reducer and mass flow controllers (Bronkhorst). The Zero Air gas flow can be adjusted from 0.5 to 6 cm^3 min^{-1} STP allowing optimization of either analytical sensitivity or instrumental response time. The use of a carrier gas improves gas exchange with seawater and its transport to the optical cavity of the MILS which markedly reduces instrument response times compared with other instruments relying solely on membrane equilibration. This configuration corresponds to an improved hybrid design as described in a recent mathematical framework describing four membrane-inlet sensor architectures (Colson and Michel, 2025). Among these designs, the hybrid configuration exhibits the fastest equilibration times, whereas passive designs - used in most commercially available sensors - are the slowest. In this study, the carrier gas flow was set to 2 cm^3 min^{-1}, corresponding to an instrumental response time of approximately 20 s at 25 °C (Grilli et al., 2018).

The total gas stream directed towards the optical cavity, comprising extracted dissolved gases, water vapor, and the carrier gas, is monitored by a mass flow controller. Under the deployment conditions in the two fjords, the mean gas flow from dissolved gases, excluding water vapor, amounts to 0.28 cm^3 min^{-1}. Data are acquired at 4 Hz and averaged over 1 s for concentration calculations, providing high-resolution CH_4 measurements suitable for fine-scale profiling in aquatic environments.

2.2.2 Deployment

The MILS was deployed either directly attached to the CTD package (Stns O4b-6b) or as close in time and space as possible to an autonomous CTD profile. The maximum time interval between the two deployments was 3.5h. Winch speeds were minimized to optimize data quality, reaching as low as 3 m min^{-1} in specific sections of the profiles. Average deployment speeds were 25.2 m min^{-1} and 12.7 m min^{-1} in 2023 and 2024, respectively. In 2023, slower deployment speeds were not possible due to winch limitations aboard *RV Sanna*. The reported average analytical uncertainty of the MILS (12%; Grilli et al., 2018) is confirmed by the mean standard deviation (15 ± 6.7%) calculated from rolling averages of the 2024 measurements (n=10796).

2.2.3 Data processing

The instrument relies on absorption spectroscopy analysis. The processed spectrum includes absorption lines for the CH_4 molecule but also for the H_2O molecule. As the calculated CH_4 concentration is referred to dry gas, it depends heavily on the water vapor variability and on the quality of its spectral fitting. Raw data were thus cleaned to filter outliers and data of low quality, usually resulting from a bad spectral fit. Detailed description of data processing is provided in the Supplementary Materials. We implemented a first step of data cleaning using key measured parameters: the spectral fit error, the water vapor concentration, and the normalized spectral signal. In a second step, we removed remaining outliers in both CH_4 and water vapor by suppressing any data point lying outside the rolling average ± k σ bounds, where σ is the standard deviation. For CH_4, we applied a 2–σ criterion using a centered rolling average on a 15–point window (7 points on either side), and for water vapor we applied a 1.8–σ criterion using a centered 100–point window. Doing this for CH_4 and water vapor, respectively filtered 2.97% and 4.85% of data observations but kept inherent variability and CH_4 structure of the vertical profiles.Once cleaned, we smoothed the water vapor time series using a 40 s moving median average to reduce high–frequency measurement noise. Data processing has been coded in python to be more easily implemented in the future.

Finally, data were corrected for environmental conditions (temperature, salinity, and dissolved oxygen) according to Grilli et al. (2018) and using CTD data and software provided by A2PS. As the embedded pressure sensor to quantify water depth suffered from an offset, we corrected this offset for each profile using the total flow measurement (drastically decreasing in contact with water) and using the observed value when the MILS was kept in standby at around 0.5m of depth before deployment. Due to the large number of MILS CH_4 measurements in each profile, we decided to depict the profiles using a moving average of 30-point window (or 30 s) and to show the 2-σ standard deviation. Due to the memory effect of the optical cavity content renewal, CH_4 measurements at a given depth are impacted by measurements performed during the preceding seconds. We thus implemented a 30-point window forward to each data point, in order to calculate the moving averages.

2.3 Discrete CH_4 analysis

Samples were collected from the Niskin bottles using a Tygon® tube and transferred into borosilicate 60 ml serum bottles. Samples were poisoned by introducing 60 mL saturated mercury chloride ($HgCl_2$) solution. The bottles were sealed with isobutyl stoppers and securely capped with aluminum crimps. The bottles were then kept in the dark at room temperature until analysis at home laboratory. Measurements of CH_4 were conducted using the headspace technique described by Weiss (1981) and Upstill-Goddard et al. (1996). Approximately 25 mL of the sea water sample was replaced by ultrapure N gas (AirLiquide Belgium®, Alphagaz 2, N2 ≥ 99.9999%), followed by manual agitation and overnight equilibration in a water bath at room temperature. A 12 mL extraction from the headspace was injected into an SRI Instrument Model 8610C Gas

Chromatograph with Electron Capture Detector, for analysis. The calibration was performed using precision gas mixtures containing N_2O, CH_4, CO_2, and N_2 provided by AirLiquide Belgium®. Average standard deviation from replicates was 7.5%.

2.4 CH_4 saturation and flux calculations

Saturation level of dissolved methane was calculated using the solubility equation from Wiesenberg and Guinasso (1979). Atmospheric CH_4 was considered according to measured concentrations at Storhofdi, Vestmannaeyjar, Iceland (63.400°N, 20.288° W, alt. 118m, June to Sept. 2023, 1986.65 ppb, n=4; June to Sept. 2024, 1995.85, n=4). Regional atmospheric CH_4 gradients at this latitude are <2 ppb based on the NOAA Global Monitoring Division network, introducing an error in flux calculations of <0.02 μmol m^{-2} d^{-1}, i.e. negligible when compared to other sources of uncertainties.

The methane sea-air flux (F) was calculated using the bulk flux equation (Wanninkhof, 2014):

$$F = k\,(CH_4\ \text{measured} - CH_4\ \text{equ.})$$

Where CH_4 measured is the concentration in water and CH_4 equ. is the air equilibrated seawater CH_4 concentration. *k* is the gas transfer velocity and is calculated based on (Wanninkhof, 2014):

$$K = aU_{10}^2(S_c/660)^{-0.5}$$

Where a is the coefficient parametrization, U_{10} is the wind speed at 10 m from the sea surface and S_c is the Schmidt number calculated following (Vogt et al., 2023) where the authors used a correction for salinity based on Jähne et al. (1987) and Manning and Nicholson (2022). The gas transfer velocity is calculated using the monthly average of the squared hourly wind speed (Wanninkhof, 2014).

Wind speed was obtained from the meteorological station ATMOS 41 Gen 2 All-in-One weather station (METER group, Pullman, USA) at the Narsaq science center at 6.75m height, covering the full duration of both field campaigns. The wind speed at 10-m height, U_{10}, can be calculated using:

$$U_{10} = U_{6.75} * (10/6.75)^{\alpha}$$

Where α is equal to 0.20 corresponding to a relatively rough surface adapted for rural-suburban area. While fjord systems differ from rural-suburban areas, the value of 0.20 falls within the range commonly applied in fjord and coastal ocean settings (e.g., Wanninkhof, 2014; Vogt et al., 2023).

Uncertainty in flux estimates was propagated from three sources: (1) CH_4 measurement uncertainty (± 15% for MILS, ± 7.5% for discrete GC), (2) wind speed uncertainty and height correction (α = 0.20 for rural conditions, with a possible overestimate of turbulence in the sheltered conditions of fjord systems), (3) uncertainty in the gas transfer parameterization. In order to assess sensitivity to the *k* parameterization, fluxes were calculated using both the Wanninkhof (2014) and Nightingale et al. (2000) formulations. Differences remained within ±30% of the mean estimate. When propagating all uncertainty sources in quadrature, total flux uncertainty is about ±55%. Episodic wind events were assessed by examining hourly wind records. No single event exceeding the monthly mean by more than a factor of two were recorded during the sampling periods. Their exclusion does not alter our qualitative conclusions. Error propagation, however, could not account for the following additional errors in flux calculation, due to the lack of available data: (1) depth-restricted methane sampling precluding to analyze the surface layer in contact with the atmosphere, (2) the lack of reliable ship-based wind measurements, (3) the lack of reference atmospheric CH_4 values on ship.

2.5 Data and statistical analyses

Data was represented using ODV (v. 5.7.2, Schlitzer, Reiner, Ocean Data View, odv.awi.de, 2025) and Sigma Plot (v.16.0). Data were explored using PCA, Pearson product moments, one-way ANOVA, and t-test using Sigma Plot (v16.0). For statistical tests, a Shapiro-Wilk normality test was conducted to define which test is appropriate. For the one-way ANOVA (t-test), with a positive normality test, a Holm-Sidak test (Mann-Whitney rank sum test) was performed, respectively. Otherwise, for the one-way ANOVA and a negative normality test, a Dunn's pairwise test was conducted.

3 Results

3.1 Oceanographic settings

Oceanographic conditions remained broadly consistent between years in both fjords (Figure 2; Supplementary Figure 2). The water column of both fjords can be divided into three main water masses based on salinity: (1) surface meltwater (<28 PSU), (2) fjord water (28–33 PSU), and (3) ocean water (> 33 PSU). This structured hydrography is used throughout in the following analyses.

Surface meltwater occupies the upper water column and is influenced by solar heating and freshwater inputs, resulting in relatively warm temperatures and low salinities, with minimum values reaching 16 PSU. Fjord water forms an intermediate layer characterized by cold temperature (1 to -1°C) and near-saturated dissolved oxygen concentrations (~90-100%, Figures 2C, D). It extends to depths of 100–150 meters in the MTG fjord. In the LTG fjord, the fjord water occupies most of the water column. Ocean water corresponds to intruding Atlantic-derived waters, characterized by high salinity, moderate temperature (~4°C) and slightly undersaturated oxygen (~90%).

In the LTG fjord, which is fed by a proglacial river draining a glacier that has retreated inland (Figure 1), surface water was warmer (up to 12°C) compared to the MTG fjord (up to 8°C, Supplementary Figure 3), consistent with stronger solar heating in absence of iceberg cooling and glacial upwelling. Salinity increased with depth in both fjords, marking the transition from surface meltwater to fjord water. This transition occurred within the upper ~5m in the LTG fjord, whereas in the MTG fjord it extended deeper (~10 m), accompanied by a temperature decrease to ~5°C (Figure 3A). This pattern is consistent with a stronger freshwater influence in the MTG fjord, likely reflecting contributions from

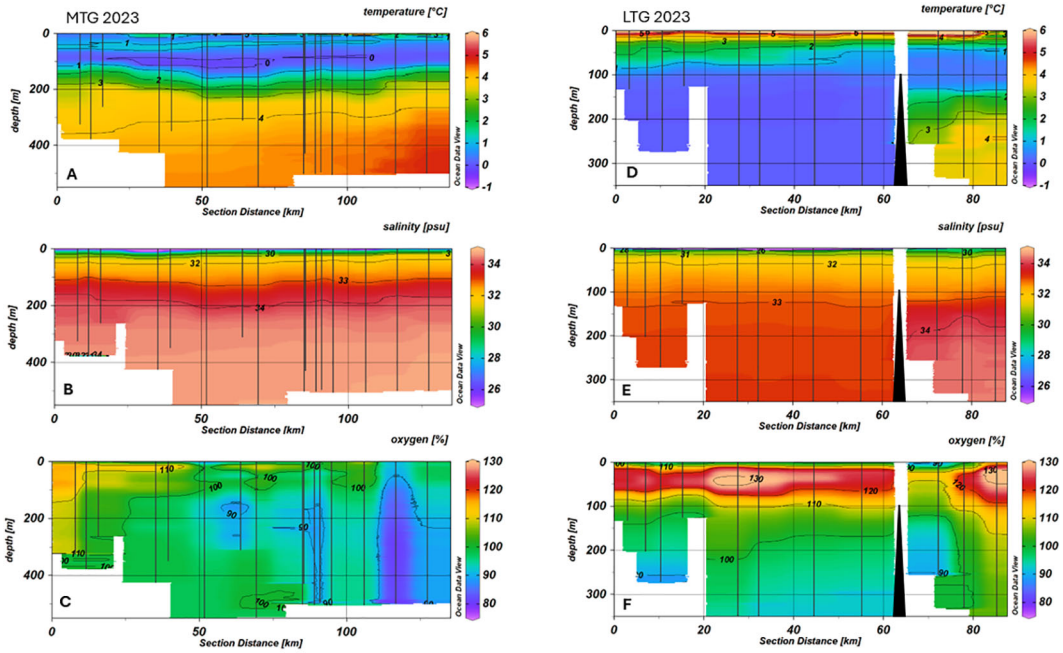

FIGURE 2
Oceanographic settings during the Greenford 2023 expeditions; showing temperature **(A, D)**, salinity **(B, E)**, dissolved oxygen (C, F, dO2, %) for both the LTG **(D-F)** and the MTG **(A-C)** fjord. Sections are represented as a function of distance from fjords' end (km 0) towards the continental plateau. The sill up to ~100 m in the LTG fjord close to Qaqortoq is shown as a black triangle up.

iceberg melt and subglacial discharge from basal meltwater and surface runoff released at the submerged glacier front. Based on Mankoff et al. (2020), the MTG drains about 1,820 km^2 of the Greenland ice sheet, while the LTG drains a catchment area of about 220 km^2. This ~8-fold difference in catchment size is consistent with a stronger freshwater signal observed in the MTG fjord. Differences between fjords are primarily expressed through the vertical extent of these water masses.

Ocean water intrudes throughout the MTG fjord, whereas in the LTG fjord its penetration is restricted by a sill near Qaqortoq

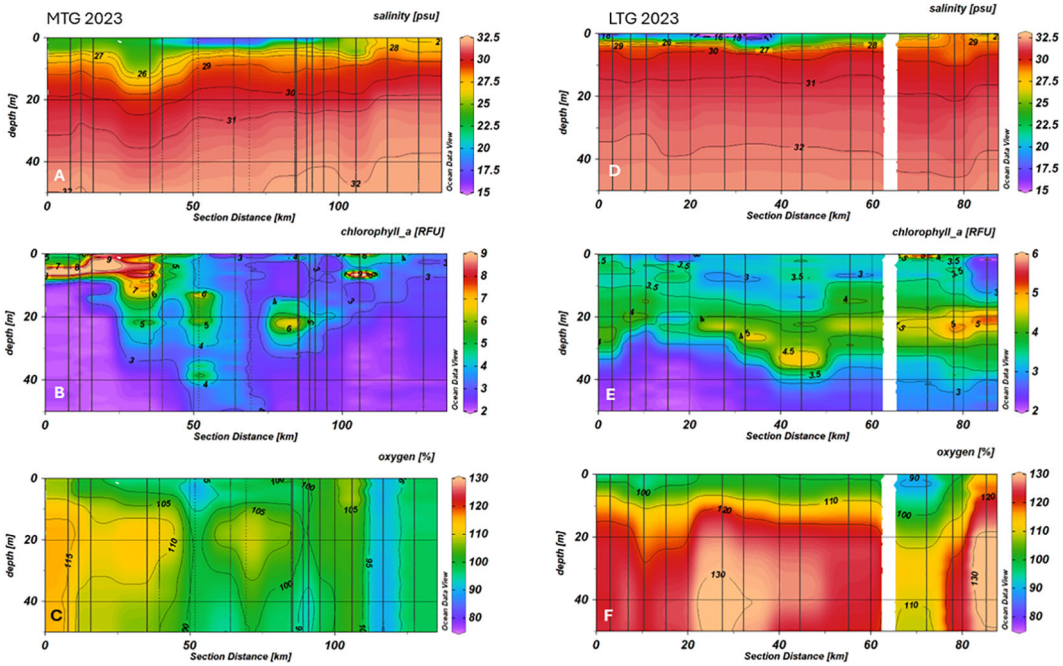

FIGURE 3
Oceanographic settings during the Greenford 2023 expeditions in the top 50 m depth; showing salinity **(A, D)**, chlorophyll_a **(B, E)**, and dissolved oxygen (C, F, dO2, %) for both the LTG **(D-F)** and the MTG **(A-C)** fjord. Sections are represented as a function of distance from fjords' end (km 0) towards the continental plateau.

(Figures 2A–D). Ocean water underlies the fjord waters, which occupy the intermediate layer between the surface meltwater and deep oceanic inflow in the MTG and the outer part of the LTG.

Together, these distinct layers, surface meltwater, fjord water, and ocean water, result in a strongly stratified water column, with sharp density gradients driven by depth-dependent variations in temperature and salinity. Differences in salinities and in the temperature profiles resulted in marked density differences between fjords (Supplementary Figure 4). Fjord water is primarily supplied by intermediate polar water, whereas ocean water originates from Atlantic-derived inflows (Straneo and Cenedese, 2015). In the MTG fjord, similar salinity thresholds are used to distinguish surface meltwater from fjord water (consistent with the definition of polar water in Straneo and Cenedese (2015).

Dissolved oxygen distributions differed markedly between the two fjords (Figures 3C, F). In the LTG fjord, oxygen supersaturation — reaching up to 130% — was observed between ~15 and 80 m depth, where temperatures ranged from 1 to 4°C. In contrast, surface waters influenced by proglacial river discharge were not oxygen supersaturated. Although Chl *a* concentrations in the LTG fjord were generally low (Figure 3E), they were consistently detectable between 10 and 30 m depth, corresponding to the upper boundary of the oxygen-rich layer. This pattern suggests that photosynthetic oxygen production, coupled with strong water column stratification, likely contributed to the elevated oxygen saturation in the LTG fjord. The influence of freshwater inputs was further assessed using the melt and runoff framework defined by Straneo and Cenedese (2015), which described the thermohaline signatures of glacially modified waters. The melt line represents mixing between ambient fjord waters and submarine meltwater, characterized by a slope of ~ 2.8 °C per unit salinity (the Gade slope), while the runoff line represents mixing between ambient water and subglacial runoff. When both submarine melt and subglacial discharge are present, water properties are expected to fall between these two lines. Applying this framework to our observations indicates that water down to depths of ~70–115 meters in the MTG fjord was affected by a combination of runoff and subglacial melt, whereas in the LTG fjord, freshwater influence was largely restricted to the upper portion of the water column (Supplementary Figure 5).

In 2023, MTG water sampling was conducted close to the glacier front (approximately 2 km from the calving front), whereas heavy ice cover prevented access to this area in 2024. At the station nearest to the glacier front (Figure 3), elevated dissolved oxygen concentrations, reduced pH (Supplementary Figure 3), and cold water temperatures were observed, consistent with the influence of subglacial meltwater derived from basal melting and submerged ice sources. Slight doming of isopycnals (Figure 3A; Supplementary Figure 4C) suggest localized upwelling of ocean-derived water near the glacier front, likely driven by buoyant subglacial discharge (Meire et al., 2017).

Collectively, these observations are consistent with the presence of subglacial meltwater input in the MTG fjord during the 2023 field campaign. Additionally, elevated Chl *a* concentrations in the upper 20 m near the glacier front (Figure 3B) further support upwelling-induced nutrient supply, consistent with previous studies demonstrating enhanced primary production associated with subglacially-driven upwelling in MTG fjords (Meire et al., 2017; Wood et al., 2025).

3.2 Comparison between MILS and discrete methane measurements

In 2024, dissolved CH_4 concentrations obtained from MILS profiles were compared with discrete measurements at five stations, spanning a concentration range of 3.2 to 8.1 nM. Overall, both methods show good agreement (Figure 4), with an average difference of 18.7 ± 12.5%, and MILS consistently reporting slightly lower methane concentrations as previously noted by Grilli et al. (2018). A linear regression between discrete and MILS measurements yields a slope of 0.828 and a R^2 of 0.962. This high level of agreement is particularly notable given that discrete sampling and MILS were conducted up to 3.5 h apart. Short-term CH_4 variability at fixed stations reaches ~1.5 nM d^{-1} (Supplementary Figure 11), which corresponds to a 17.5 to 26.5% variability at 5, 70 and 120 m of depth. Hence, a 3.5-hour lag could possibly account for a concentration difference of ~0.2 nM. Hence, probably the observed 18.7% difference between discrete and MILS data can be attributed to the instrumental response as well as to temporal variability.

Good agreement was also observed when MILS profiles were overlaid with discrete measurements (Figure 5; Supplementary Figure 6). In most cases standard deviations of the two methods overlapped, and both approaches revealed consistent vertical patterns, with higher CH_4 concentrations in surface waters and lower concentrations at depth (Figure 5). This coherence further supports the reliability of the MILS measurements for resolving fine-scale CH_4 distributions.

In 2023, an earlier prototype of the MILS was deployed at five stations in each fjord. However, quantitative agreement with discrete samples was poorer, limiting interpretation of the 2023 dataset to qualitative comparisons at selected stations. On average,

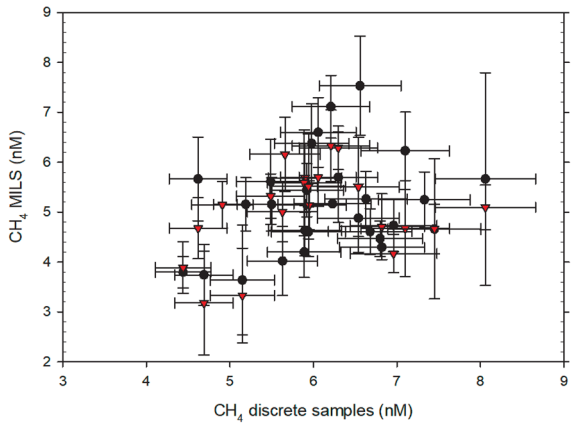

FIGURE 4
Comparison between discrete and MILS dissolved methane concentrations for 2024. Data are from surface to deep water (A, n=49), upcast (black circle) and downcast (red triangle down). MILS data are shown. Error bars represent standard deviations. The solid line represents a 1:1 line, whereas the dotted line represents the linear regression between MILS and discrete data.

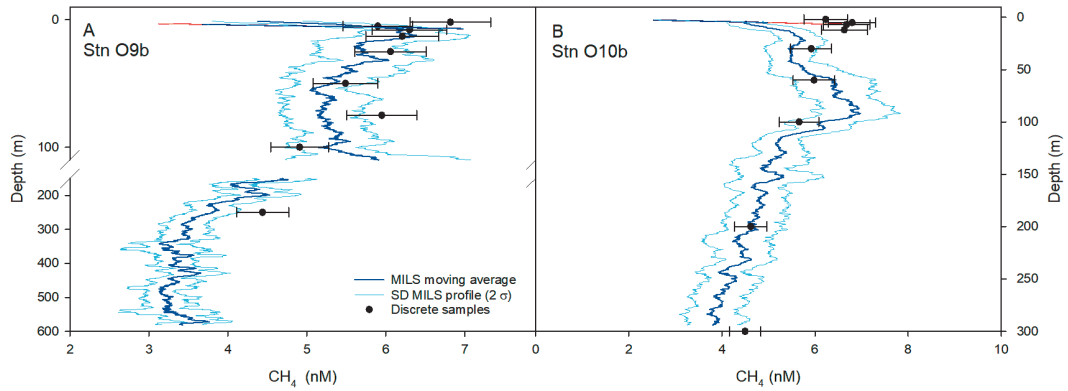

FIGURE 5
MILS profile overlaid to discrete values for selected stations (O9b, **A**; O10b, **B**). As the MILS records CH_4 every second, to ease profile visualization, MILS profiles are represented considering the moving average values with a 30 sec forward data acquisition. Standard deviation was calculated on this moving average. Data gap at Stn O9b **(A)** represents depths for which no data was collected due to poor spectral fit. Error bars represent the average standard deviation on discrete samples.

CH_4 concentrations measured by the 2023 MILS prototype were 48 ± 12% lower than those obtained from discrete samples (n = 65, Supplementary Figure 7). This difference is attributed to a drift in the gas flow measurement, because the instrument could not be recalibrated immediately following the 2023 expedition, and this bias could not be corrected retrospectively. Due to the unresolvable bias in the 2023 MILS data, these profiles are excluded from all quantitative analyses. They are retained solely for qualitative assessment of vertical structures and inter-station patterns (Supplementary Figure 8). Consistent patterns were observed when comparing the MILS prototype deployed in 2023 with discrete measurements, showing higher CH_4 concentrations in surface waters and generally elevated CH_4 levels in the MTG fjord compared to LTG fjord (Supplementary Figure 8).

The MILS provided unique information not accessible from discrete sampling. Firstly, high-resolution MILS profiles at Station O1, ~2km from the calving front, and above the pockmark of Station O11, showed no detectable CH_4 anomaly at any depth, conclusively ruling out significant methane release at these locations. Such findings would have required a hardly-deployable discrete sampling grid to reach a similar conclusion. Secondly, the MILS profiles revealed localized areas of elevated CH_4 (~0.5 to 1 nM above background) between 50 and 100 m depth at specific stations in the MTG fjord, that would not have been resolvable with the depth resolution of the discrete sampling. Thirdly, the MILS profiles confirmed that no fine-scale vertical structure was missed by discrete sampling in other sections of the water column, thus bringing confidence in the overall fjord-scale CH_4 distributions derived from discrete samples.

3.3 Methane discrete data

Because MILS data were collected at only a limited number of stations following instrument failure in the LTG fjord in 2024, we primarily rely on discrete measurements to compare CH_4 distributions between both fjords and assess interannual variability between 2023 and 2024. Overall, dissolved CH_4 concentrations remained within a narrow range, spanning 4.43 - 9.30 nM in 2023 and 4.07 - 8.06 nM in 2024 (Figure 6). Methane concentrations are presented according to the three main water masses identified in the fjords: surface meltwater (< 28 PSU), cold fjord water (28 to 33 PSU) and warmer ocean water (> 33 PSU).

In the MTG fjord (Figure 6), CH_4 distributions are described first for 2023, then for 2024, followed by an interannual comparison. In 2023, CH_4 concentrations were highest in surface meltwater (7.25 ± 0.91 nM, n=12), decreased in fjord water (6.28± 0.88 nM, n = 28, p = 0.043), and were lowest in ocean water (5.01 ± 0.34 nM, n = 10). The highest values in surface meltwater occurred in the central section of the fjord (Figures 6A, C). In 2024, CH_4 concentrations remained similar between surface meltwater (6.17 ± 0.76 nM, n = 13) and fjord water (6.24 ± 0.83 nM, n = 48), but were significantly lower in ocean water (4.59 ± 0.36 nM, n = 15). Interannual comparison indicates that CH_4 concentrations were broadly comparable within each water mass, except in surface meltwater where concentrations were significantly higher in 2023 (p = 0.004). These results indicate that CH_4 concentrations were generally highest in surface meltwater and decreased with depth across both years. A side fjord sampled in 2023 shows CH_4 distributions consistent with those observed in the main MTG fjord.

Near the glacier calving front (Stn O1, Figure 1), dissolved CH_4 concentrations were slightly lower than those measured at stations farther west within the fjord (Figure 3A), indicating no detectable CH_4 input associated with subglacial meltwater at this location. Elevated surface CH_4 concentrations persisted toward the fjord mouth (Stns O15 and O12b). Over the shallow continental shelf (Stn O13b) surface CH_4 concentration declined, whereas higher concentrations were found at depth.

In the LTG fjord, results are presented following the same structure, with 2023, then 2024, and interannual comparison. In 2023, CH_4 concentrations decreased with depth across the three water masses, with mean values of 5.87 ± 0.29 nM (n=4) in surface meltwater, 6.14 ± 0.61 nM (n=17) in fjord water, and 5.42 ± 0.54 nM (n=8) in ocean water. In 2024, CH_4 concentrations were similar in surface meltwater (5.79 ± 0.83 nM, n=7) but lower in fjord water (5.67 ± 0.64 nM, n=31) compared to 2023 (p = 0.0495). Ocean water concentrations remained low (5.33 nM, n=1).

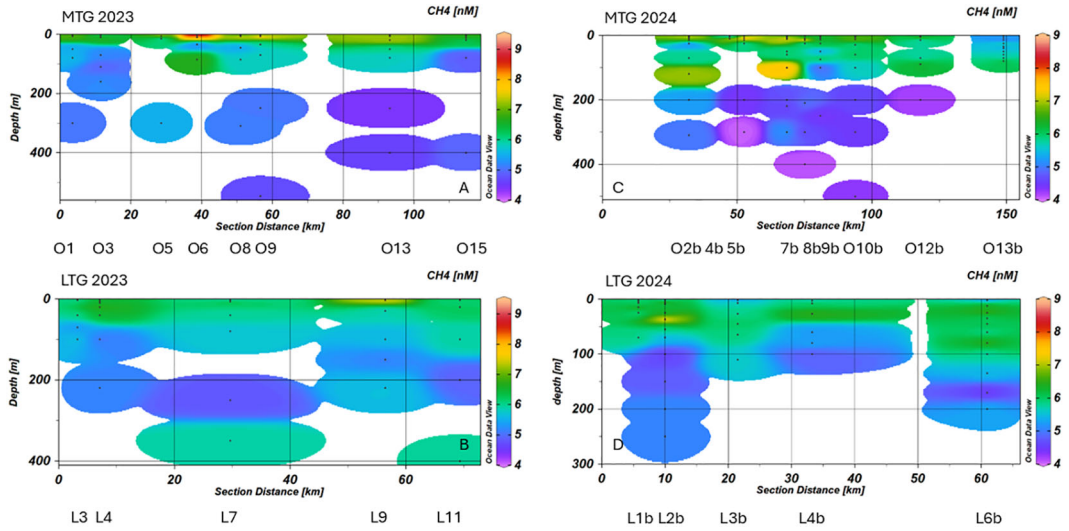

FIGURE 6
Methane concentrations in the MTG **(A, C)** and the LTG **(B, D)** fjords in 2023 **(A, B)** and 2024 **(C, D)**.

The LTG fjord generally exhibited slightly lower CH_4 concentrations in surface meltwater compared to the MTG fjord, although this difference was statistically significant only in 2023 ($p = 0.404$ for 2024). Relative to the MTG fjord, the LTG fjord exhibited slightly higher methane concentrations in the intermediate (50–120 m) layer and near the seafloor (Stn L7 and L11, Figure 6B). In 2024, elevated CH_4 concentrations extended deeper into the water column than in 2023, reaching depths of ~100 m (Figure 6D). Mean CH_4 concentrations for each water mass are summarized in Figure 7.

Differences between measured dissolved CH_4 concentrations and calculated concentrations at equilibrium with the atmosphere for the 0–3 m depth range indicate consistently higher mean CH_4 excess in the MTG than in the LTG, yet this difference is not statistically significant. In 2024, the mean excess was 2.15 ± 0.76 nM (n=10) in the MTG fjord and 1.83 ± 0.29 nM (n=4) in the LTG fjord. In 2023, CH_4 excess were higher overall, averaging 3.10 ± 1.07 nM (n=7) in the MTG fjord and 2.76 ± 0.81 nM (n=5) in the LTG fjord. Stations located in the side fjord (Stns O16 and O19) exhibited comparable CH_4 excess values (3.22 and 3.76 nM, respectively) to those observed in the main MTG fjord in 2023. Methane saturation in surface meltwaters in the MTG fjord was at 161 ± 20.0% and 182 ± 22.0% for 2023 and 2024, respectively. It was on average 173 ± 28.2% in surface meltwater of the LTG fjord.

Calculated sea-air fluxes were low. In 2023, fluxes in the MTG ranged from 0.49–1.11 μmol m^{-2} d^{-1} (n=7) comparable to those measured in the adjacent side fjord (0.80 μmol m^{-2} d^{-1}, n=2). Mean CH_4 fluxes were slightly higher in the MTG fjord (0.77 μmol m^{-2} d^{-1}) than in the LTG fjord (0.56 ± 0.08 μmol m^{-2} d^{-1}, n=5; p=0.02). In 2024, stronger wind conditions resulted in significantly higher CH_4 fluxes which were statistically indistinguishable between the LTG (2.13 ± 0.29 μmol m^{-2} d^{-1}, n=5) and MTG fjords (2.04 ± 0.81 μmol m^{-2} d^{-1}, n=5). Overall, CH_4 fluxes across both fjords ranged from 0.49 to 3.31 μmol m^{-2} d^{-1} during these two field campaigns. Flux

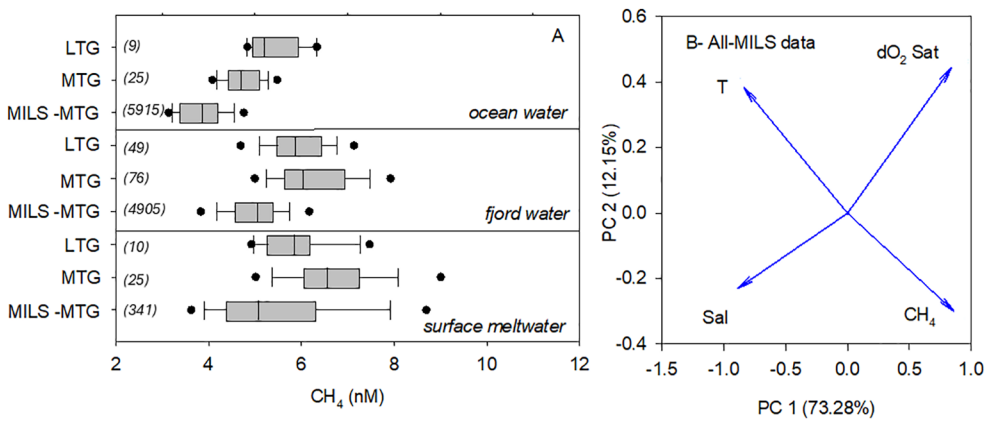

FIGURE 7
Methane concentration in the three layers **(A)** for 2024 showing MILS data and discrete data (2023 and 2024) for the MTG (and side fjord) and LTG fjords. Number of observations are shown in brackets. PCA from the MILS data in the MTG fjord (**B**, n=10796, all depths). Data are represented as a box plot showing median and 5th, 95th percentile. Ocean water, fjord water and surface meltwater were defined with salinity greater than 33 PSU, between 28 and 33 PSU, and below 28 PSU, respectively.

variability relative to *k* parameterization alone may lead to uncertainties of ±55%, while error on methane measurements can lead to uncertainties of ±30%. Using monthly averaged wind speeds may not fully capture episodes of higher fluxes. Hence, flux values given here should be interpreted as orders of magnitude rather than precise constraints.

3.4 Methane relationship with physical drivers

Relationships between CH_4 and environmental parameters were assessed using Pearson correlation analyses (Supplementary Tables 2, 3, significance level p = 0.05) and principal component analysis (PCA). Across both fjords, CH_4 concentrations exhibited a consistent and statistically significant negative correlation with depth, with stronger correlations in the MTG fjord (R = -0.63 to -0.64) than in the LTG fjord (R = -0.46 to -0.51). Temperature-CH_4 relationships differed markedly between both fjords: in LTG fjord, temperature was either positively correlated with methane (R = 0.43) or showed no significant relationship (p = 0.809 in 2024). In contrast, CH_4 concentrations in the MTG fjord were negatively correlated with temperature in both years (R = -0.37 and -0.34 for 2023 and 2024, respectively). A similar contrast was observed for salinity; no significant correlation with CH_4 was detected in the LTG fjords (p = 0.244 in 2024; p = 0.719 in 2023), whereas CH_4 was negatively correlated with salinity in the MTG fjord (R = -0.68 in 2024; R = -0.46 in 2023).

Incorporating 2024 MILS data from the MTG fjord, which was calibrated against discrete measurements, into the water mass analysis substantially improved spatial resolution, from ~5–10 m discrete depth intervals to 1-s continuous profiles at ~0.2 m vertical resolution at the mean deployment speed of 12.7 m min^{-1} (Supplementary Figure 9), allowing for more robust assessment of relationships between CH_4 and environmental parameters. Consistent with the discrete dataset, CH_4 concentrations in surface meltwater were not statistically different from those in fjord water (p = 1.00), while concentrations in ocean water were significantly lower than in both surface meltwater and fjord water (p < 0.001, Figure 7A).

4 Discussion

Dissolved CH_4 distributions were remarkably similar between 2023 and 2024 with statistically significant interannual differences limited to two cases: slightly higher CH_4 concentrations in surface meltwater of the MTG fjord in 2024 (by 1.08 nM on average) and higher CH_4 concentrations in fjord water of the LTG in 2023 (by 0.47 nM on average). These modest differences are likely influenced by the timing of the sampling campaigns. In 2023, sampling was conducted at the end of the melt season (23 August - 3 September), whereas in 2024, measurements were collected earlier in summer (3–21 July), corresponding approximately to the onset of the seasonal melt (Gräff et al., 2025; Hansen et al., 2025). Moreover, 2024 was characterized by anomalous climatic conditions marked by extensive ice discharge into the ocean but reduced overall ice-sheet melt, driven by persistent low-pressure systems and northerly winds over southwest Greenland (Poinart et al., 2024). Despite these contrasting seasonal and meteorological conditions, CH_4 concentrations remained within a narrow range across both fjord types. Considering the observed short-term variability in CH_4 concentrations, reaching up to 1.5 nM on daily timescales (Supplementary Figure 11), the overall CH_4 distributions in both the MTG and LTG fjords can be considered broadly similar between years.

Methane was supersaturated throughout the water column in both fjords yet concentrations were lower than those previously reported for several other Arctic fjords in Svalbard (2–240 nM, Damm et al., 2005; 10–23 nM, Damm et al., 2021; 20–72 nM, Mau et al., 2013). At the same time, CH_4 concentrations reported here exceeded values reported for Greenland shelf meltwater (3.8-5.4 nM) and winter mixed layers (4.2-5.6 nM; Verdugo et al., 2022). These observations place southwestern Greenland fjords as relatively weak methane sources within the Arctic system, compared to seep-influenced fjords (e.g., Svalbard), but slightly enriched compared to open-shelf waters.

In contrast to Svalbard fjords, where active seafloor gas seepage dominates CH_4 distributions (Rodes et al., 2023), CH_4 concentrations in our study decrease with depth. Surface meltwater and fjord water consistently exhibited higher CH_4 concentrations than underlying ocean water, with average saturation levels of ~171% and 156%, respectively, across the full length of both fjords. Methane was preferentially distributed along pycnoclines as previously reported in other fjord systems (Damm et al., 2005), suggesting lateral transport and retention along density interfaces.

Considering reported along-fjord flow velocities of up to ~0.8m/s in the MTG fjord (Straneo and Cenedese, 2015) and fjord lengths of approximately 110 km (MTG) and 75 km (LTG) (Figures 1, 2), surface meltwater would be transported from the fjord head to the mouth within 26 to 38 h, respectively. The persistence of elevated CH_4 concentrations over these spatial and temporal scales therefore implies the presence of sustained CH_4 sources enriching surface meltwater and fjord water, rather than a single localized input.

Near Qaqortoq, a sill prevents the intrusion of ocean water with low CH_4 concentrations and affects fjord circulation in the LTG fjord which might not be widely representative of LTG fjords. However, the high similarity of CH_4 concentrations in the surface meltwater and fjord water in both the MTG and LTG fjords, support the representativeness of our LTG fjord to discuss CH_4 distributions in summertime.

4.1 Methane sources

Potential terrestrial CH_4 sources relevant to the study region are documented and include multiple pathways associated with melting of the Greenland ice sheet (Christiansen and Jørgensen, 2018; Lamarche-Gagnon et al., 2019). Meltwater enriched in CH_4 may be delivered to fjord systems via (i) basal meltwater released either as a subglacial plume in the MTG fjords or routed through proglacial rivers in the LTG fjords, (ii) meltwater from submerged glacier ice and icebergs, which may carry dissolved CH_4 from bubble inclusions, though a likely minor contribution compared to subglacial discharge, and (iii) surface melt and runoff draining

the ice sheet, which, however, is more CH_4-depleted than the other pathways due to dissolved CH_4 transfer to the atmosphere during transit (Strock et al., 2024; Gräff et al., 2025; Hansen et al., 2025).

Indeed, extremely high CH_4 concentrations were reported near subglacial meltwater outlets (average 271 nM; Lamarche-Gagnon et al., 2019), demonstrating the potential for glacial CH_4 release. However, substantial CH_4 losses during downstream transport have been documented (Lamarche-Gagnon et al., 2019; Strock et al., 2024). In particular, surface runoff and proglacial rivers experience significant CH_4 loss through atmospheric release and microbial oxidation (Lamarche-Gagnon et al., 2019; Strock et al., 2024). Oxidation alone has been shown to reduce CH_4 fluxes by ~53% over distances of ~4km, comparable to the transport distance between the glacier margin and fjord entry in the LTG system investigated here (Figure 1). Under these conditions, CH_4 delivered to the LTG fjord via proglacial runoff would be strongly attenuated prior to entering the fjord. Consequently, the relatively low CH_4 concentrations observed near the proglacial river input in the LTG fjord (5–6 nM) are consistent with substantial pre-fjord CH_4 loss and do not indicate a strong direct CH_4 source at fjord scale. Recent observations at the EKaS glacier in the MTG fjord has revealed elevated buoyancy frequencies within the upper 50 m near the glacier front in 2023, likely associated with subglacial meltwater plume (Gräff et al., 2025). EKaS is grounded well below sea level, reaching depths of ~300 m (Gräff et al., 2025). It drains approximately 0.3% of the Greenland ice sheet, and is associated with an annual ice discharge of ~3 $km^3\ yr^{-1}$ (Gardner et al., 2022). Ice flow velocities at the calving front range from ~15 m d^{-1} in late spring to 5 m d^{-1} by late summer (Gräff et al., 2025). If subglacial discharge were associated with substantial basal CH_4 release, markedly higher CH_4 concentrations than those observed here would be expected in close proximity to the glacial front. In 2023 we sampled as close as ~ 2 km from the calving front. Nevertheless, concentrations measured at O1 in 2023 showed no detectable enrichment attributable to basal melt input, suggesting that basal melting is not a major CH_4 source in the MTG fjord during summertime, within the spatial resolution of our observations.

Using salinity and freshwater contribution, a simple dilution calculation corroborates this conclusion. Basal meltwater accounts for ~20% of total freshwater input in July and ~25-50% in August-September (Hansen et al., 2025). With the upper estimate of 271 nM of CH_4 in subglacial discharge (Lamarche-Gagnon et al., 2019), and assuming that this discharge conservatively mixes into the fjord water mass (having a salinity of 28–33 PSU), leading to a dilution factor of the order of 50, the expected CH_4 contribution from basal meltwater sources would total ~5 nM, i.e. a comparable value to background concentrations in intruding Atlantic water. Such estimate, neglecting oxidative loss (which would further decrease this number), demonstrates that fjord-scale dilution alone is sufficient to make subglacial CH_4 indistinguishable from background level. The absence of subglacial CH_4 enrichment at Stn O1 is therefore consistent with dilution rather than implying an absence of subglacial CH_4 discharge.

CTD observations do, however, reveal physical signatures of subglacial influence, including doming of pycnoclines and a slightly elevated temperature anomaly (~1° °C) at ~50 m depth which extends over ~100 km (Figure 2), attesting for ocean water upwelling and mixing with glacially modified waters. Freshwater inputs indeed affected the upper 70–110 m of the water column in 2023, and subglacial discharge was independently identified through trace element distributions (e.g. Mg and Pb; Castrillejo Iridoy et al., in prep.). In addition, stepwise pycnocline formed near the glacier front as a result of iceberg calving (Gräff et al., 2025). Such stratification may temporarily retain dissolved CH_4 release locally and delay its vertical or lateral dispersion.

On average, CH_4 concentrations in surface waters were 0.38 - 1.38 nM higher in the MTG fjord compared to the LTG fjord, yet this difference was only statistically significant in 2023 (p=0.404 in 2024). Overall low CH_4 concentrations in both fjords are consistent with the dominance of surface runoff freshwater delivery in summer, as recently quantified by Hansen et al. (2025) for the EkaS catchment. In this case, most CH_4 is expected to be lost by diffusion (Kleber et al., 2025) and microbial oxidation (Mao et al., 2022) prior to entering the fjord. Although total meltwater discharge peaks in summer, the fraction derived from basal meltwater is lowest at this time (~20% in July, compared to ~25-50% in August-September; Hansen et al., 2025), limiting the potential contribution of CH_4-rich basal waters to the fjord during the summer. As the dominant surface runoff loses most of its CH_4 through atmospheric evasion before reaching the fjord, the net effect is CH_4-depleted freshwater inputs despite high total discharge. The slightly elevated CH_4 concentrations observed in the MTG fjord compared to the LTG fjord may be attributed to localized inputs from iceberg melt rather than enhanced CH_4 release, as icebergs can carry dissolved CH_4 from bubble inclusions (Damm et al., 2021), although this source has not been directly quantified in Greenland settings. In contrast, the similarly low CH_4 concentrations observed in both fjords are consistent with a dominant influence of surface runoff feeding both systems. The larger differences between MTG and LTG 2023 CH_4 concentrations may reflect a greater relative contribution of basal meltwater input at the end of melt season, when basal melting represents a larger fraction of total freshwater input. Basal meltwater has previously been identified as a potential CH_4 source beneath the Greenland ice sheet (Christiansen and Jørgensen, 2018; Lamarche-Gagnon et al., 2019), providing a plausible explanation for the enhanced MTG-LTG contrast in late summer.

Sea-ice can act as both a source of CH_4 and a barrier to sea-air exchange (Damm et al., 2015; Verdugo et al., 2022). The southern Greenlandic fjords studied here are typically ice-free in summer. However, in 2024 extensive sea-ice coverage persisted over the adjacent shelf and intruded into both fjords, delaying the arrival of RVs Forel and Sanna to Narsaq. Because our sampling was conducted during the period of sea-ice retreat, CH_4 levels in surface meltwater and fjord water were relatively homogenous. This pattern is consistent with reduced sea-air CH_4 exchange under partial ice cover, which would limit CH_4 loss to the atmosphere and promote retention within the upper water column.

In the MTG fjord, high-resolution MILS profiles showed localized pockets of elevated CH_4 concentrations between ~50-100m depth (Figure 3B), suggesting discrete subsurface inputs, possibly associated with groundwater discharge (Kleber et al.,

2023), sedimentary release associated with microbial activity within anaerobic microenvironment of entrained particles (Plough et al., 1997), or release of CH_4 accumulated in sediments (Borges et al., 2016). However, the absence of stable isotope measurements, together with limited constraints on freshwater budgets, bathymetry and circulation patterns in the fjords, precludes definitive source attribution. An additional potential source is lateral input from side fjords, several of which drain retreating glaciers (e.g., Stn O16 and O19 in 2023). Methane concentrations in the sampled side fjord were indeed slightly higher (6.95 ± 0.77 nM, n=9) than those observed in the MTG fjord. Alternatively, CH_4 accumulation at depth may result from physical trapping within the strongly stratified water column (Damm et al., 2021). In particular, CH_4 release from melting icebergs in the MTG fjord known to have deeply submerged keels (sometimes exceeding 100m); melting at these depths could release freshwater and CH_4 that become trapped along density interfaces (Straneo and Cenedese, 2015) which could explain such localized subsurface methane accumulation.

The LTG fjord is comparatively shallower with water depths decreasing from ~400 m near station L1 to ~145 m near station L9. At several stations, CH_4 concentrations were elevated near the seafloor (e.g. L7 in 2023), a pattern also observed over the shallow continental shelf (Stn O13b, 2024). A substantial fraction of sedimentary CH_4 is efficiently oxidized before reaching the overlying water column. Mau et al. (2013) demonstrated that up to ~80% of CH_4 produced in Arctic sediments can be lost through anaerobic oxidation with additional losses occurring by aerobic microbial oxidation at the sediment-water interface (Reeburgh et al., 2007). More recently, Szymczycha et al. (2025) showed that organic matter production at depth in Arctic fjords can further stimulate microbial CH_4 consumption, thereby reducing CH_4 release at depth.

Enhanced near-bottom CH_4 concentrations are widely reported in the Arctic Ocean (Lorenson et al., 2016; Kudo et al., 2018) and Arctic fjords (Damm et al., 2005; Mau et al., 2013; Damm et al., 2021), where they are commonly attributed to CH_4 seepage (Damm et al., 2005) or sedimentary microbial methanogenesis (Damm et al., 2007). In these systems, CH_4 concentrations are much higher than those observed here. Therefore, in the fjords investigated here CH_4 inputs from the seabed can be excluded. Although diffuse sedimentary inputs cannot be entirely ruled out, given the occurrence of localized deep CH_4 enrichments, no evidence was found for focused CH_4 release from the seafloor. In the MTG fjord, sampling depth was limited to 550 m by operational constraints of our CTD, while maximum fjord depths reach ~680 m based on echo sounder data. Nevertheless, a MILS profile collected close to the seabed (Stn O11 in 2023), directly above a pockmark identified in our bathymetry survey, did not reveal any CH_4 input. In contrast, on the continental shelf, a clear methane enrichment at depth was observed, consistent with previous observations from the Greenland shelf (Kitidis et al., 2010), Svalbard shelf (Damm et al., 2005), and the east Siberian shelf (Vinogradova et al., 2022).

In summary, the results presented above point to multiple weak and diffuse CH_4 sources in both fjords, with no single dominant pathway. Subglacial CH_4 is likely present but diluted to background levels when entering the fjord. Iceberg melt may contribute locally. And surface run-off, while dominating freshwater input during summer, carries CH_4-depleted water. Such combination can explain the uniformly low and similar CH_4 concentrations observed across both fjord types. Surprisingly, no significant CH_4 input from the seabed was detected within the fjords themselves, in contrast to the adjacent continental shelf, where clear near-bottom enrichment was observed (Stn O13b), consistent with CH_4 concentrations reported for Greenland shelf waters (Verdugo et al., 2022). Surface meltwater exported from these fjords appears to represent only a marginal source of CH_4 to nearby shelf waters. Together, these findings indicate that, despite ongoing glacier retreat and freshwater input, southern Greenland fjords remain weak contributors to regional marine CH_4 budgets. Our observations are limited, however, to summer conditions, when surface meltwater discharge dominates freshwater inputs and subsequent stratification. Under such conditions, subglacial methane inputs may be rapidly diluted or oxidized before becoming detectable at the scale of the fjords. Seasonal variability, including winter mixing, may affect methane dynamics and should thus be the focus of further investigations.

4.2 Salinity-driven loss controls CH_4 distribution at depth

Principal component analysis of the 2024 MILS dataset explained 85% of the total variance within the first two principal components (PC1 and PC2), indicating a strong representation of the underlying data structure (Figure 7B). The PCA results show no direct association between CH_4 concentrations and physical drivers. The lack of coupling persisted when surface meltwater, fjord water and ocean water were analyzed separately (Supplementary Figure 10), further supporting the conclusion that CH_4 distributions are not primarily controlled by physical drivers within individual water masses.

Although CH_4 concentrations do not exhibit a simple linear relationship with any single physical driver when the full dataset is considered, a systematic and consistent dependence on water-mass identity (defined by salinity thresholds) is apparent. This indicates that water-mass mixing rather than continuous gradients in temperature and salinity drives CH_4 variability. This pattern is consistently observed across both fjords and both sampling years and is further supported by the high-resolution MILS data (Supplementary Figures 7, 9). Still, CH_4 distributions in the MTG fjord are more strongly influenced by water-mass structure and mixing processes than in the LTG fjord. This difference is consistent with the pronounced intrusion of saline ocean water observed in the MTG fjord, which is largely absent in the LTG fjord due to the sill preventing ocean water intrusion near Qaqortoq (Figure 2).

At intermediate depths where the salinity transition occurs (<7–10 m in the MTG fjord and <15–20 m in the LTG fjord), a negative slope is observed between CH_4 concentrations and salinity in both systems (Figure 8). Similar slopes were observed for both years and fjords (-0.55 and -0.63 nM CH_4 PSU^{-1} for the LTG, -0.33 and -0.40 nM CH_4 PSU^{-1} for the MTG in 2023 and 2024, respectively), suggesting a systematic CH_4 loss term that scales with salinity. This behaviour suggests that CH_4 is progressively removed as waters transition from fresher to more saline conditions.

Two mechanisms likely contribute to this apparent loss term: (i) aerobic CH_4 oxidation within fjord waters, as documented in similar

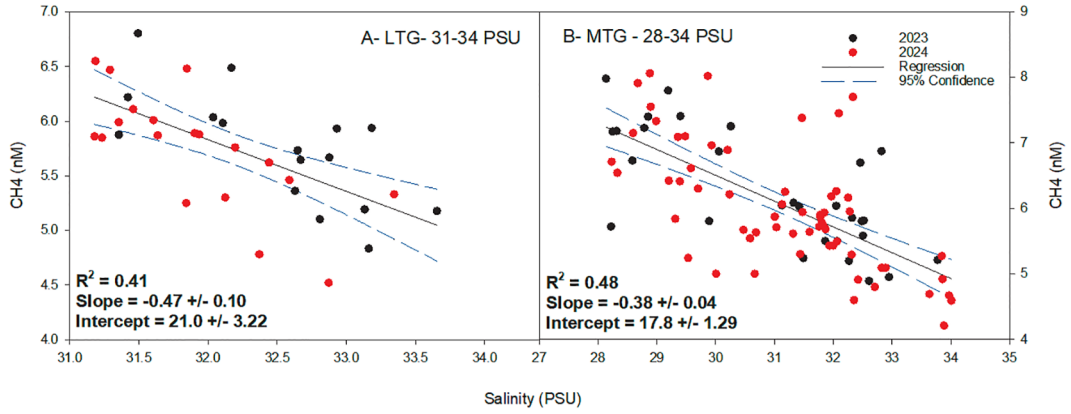

FIGURE 8
Relationship with salinity observed in the LTG **(A)** and MTG **(B)** for both years. Linear regression line and 95% confidence along with its equation are shown. Salinity below 31 PSU corresponds to surface meltwater and the shallow layer of the fjord water (down to 15–20 m) in the LTG fjord. Salinity below 28 PSU corresponds to surface meltwater (down to 7–10 m) in the MTG fjord.

Arctic settings (Mau et al., 2013), which would preferentially reduce CH_4 concentrations as waters mix laterally and vertically; (ii) dilution by intruding low-CH_4 ocean waters, which reduces concentrations within the fjord without removing methane from the ocean-atmosphere system. We note that dilution does not constitute a true CH_4 sink but acts as an apparent loss term in the fjord water column. Arctic Intermediate Water on the Greenland shelf (salinity > 34.4 PSU) contains relatively low CH_4 concentrations (1.8 to 4.0 nM; Verdugo et al., 2022) and its mixing with fjord waters would lower CH_4 levels.

The relative importance of these processes likely differs between fjords due to contrasting circulation regimes. In the LTG fjord, a sill restricts ocean water intrusion (Figure 2), leading to longer deep-water residence times, ranging from months to decades (Straneo and Cenedese, 2015). In contrast, the MTG fjord lacks a sill and experiences enhanced ocean-water intrusion fueled by glacial freshwater discharge, resulting in shorter deep-water residence times (Figure 2) (Straneo and Cenedese, 2015). Despite this, the inferred CH_4 loss term per unit salinity is greater in the LTG (0.47 nM CH_4 PSU^{-1}) compared to the MTG fjord (0.38 nM CH_4 PSU^{-1}, Figure 8), suggesting that prolonged residence times in the LTG fjord may enhance cumulative CH_4 removal through oxidation and mixing processes.

Using a CH_4 oxidation rate of 0.032 nM d^{-1} reported for Arctic fjords (Mau et al., 2013), the expected oxidative loss for a CH_4 concentration of 5 nM would be 0.16 nM d^{-1}. This rate is comparatively slow and therefore unlikely to dominate the CH_4 loss. Consequently, aerobic oxidation alone cannot account for the systematic decrease in CH_4 concentrations with increasing salinity and depth.

Figure 8 shows the key findings of this regression analysis between CH_4 and salinity. In both fjords and both years, dissolved CH_4 concentrations increase systematically with decreasing salinity in the intermediate depth range, with similar slopes across all conditions. This pattern brings the main evidence for a salinity-driven loss term governing CH_4 distributions at depth. The following discussion addresses its mechanistic basis. The consistent decrease in CH_4 at higher salinities and greater depth does not seem to be compatible with diffuse sedimentary CH_4 input, which would be expected to produce increasing CH_4 concentrations toward the seafloor. Pro-glacial groundwater discharge at depth (Kleber et al., 2023) followed by dilution by ocean-water intrusion could in principle explain the observed patterns. However, high-resolution MILS profiles did not reveal localized CH_4 maxima at depth that would be indicative of focused groundwater inputs.

An alternative explanation is the existence of an effective CH_4 concentration threshold below which further microbial oxidation becomes inefficient (Verdugo et al., 2022). Such a threshold may depend on salinity or water-mass properties, potentially contributing to the observed CH_4-salinity relationship. Disentangling these mechanisms would require additional tracers, particularly stable carbon isotopes/$\delta^{13}C$-CH_4), combined with improved constraints on water mass dilution driven-processes, oxidation-limited regimes and subtle subsurface CH_4 sources.

4.3 Methane flux to the atmosphere in a climate change scenario

Diffusive CH_4 fluxes measured in both fjords were low, ranging from 0.49 to 3.31 μmol m^{-2} d^{-1} and broadly comparable. These fluxes are similar to those reported for the Chukchi Sea (1.1–2.4 μmol CH_4 m^{-2} d^{-1}; Ye et al., 2023), but substantially smaller than those observed in the Beaufort Sea (8.8–27 μmol CH_4 m^{-2} d^{-1}; Lorenson et al., 2016). Importantly, CH_4 emissions from both fjords are orders of magnitude smaller than other CH_4 sources associated with glacial environments, including meltwater at discharge of glacier outlets (e.g., $15x10^3$ μmol CH_4 m^{-2} d^{-1}; Lamarche-Gagnon et al., 2019), pro-glacial rivers (63 μmol CH_4 m^{-2} d^{-1}; Strock et al., 2024), or groundwater discharge (6.33 μmol CH_4 m^{-2} d^{-1}; Kleber et al., 2023).

The low CH_4 concentrations and fluxes observed here are consistent with substantial CH_4 loss occurring prior to fjord entry. Freshwater discharge to these fjords is dominated during summer by surface runoff (Hansen et al., 2025), during which CH_4 is efficiently lost through atmospheric evasion and microbial oxidation before reaching the fjord system. Furthermore, the presence of a low-salinity meltwater surface layer and strong summertime stratification further suppresses vertical mixing and limit sea–air gas exchange (Damm et al., 2021; Verdugo et al., 2022).

Overall, our study showed that southwest Greenland fjords represent a relatively weak source of atmospheric CH_4 in summertime. The lack of a clear difference in CH_4 fluxes between MTG and LTG fjords in this specific setting implies that glacier retreat associated with ongoing climate change is unlikely to substantially alter summertime fjord CH_4 emission in southern Greenland. However, this conclusion is seasonally constrained. Wintertime measurements, when surface runoff is absent, would be critical to assess whether basal and submerged glacier melt could contribute more significantly to CH_4 accumulation, and atmospheric fluxes under different hydrographic conditions.

Overall, future campaigns covering additional fjord systems across the Greenland coasts, combined with wintertime measurements, would be needed to support reliable regional CH_4 budget estimates. Emerging approaches, including autonomous and remote sampling platforms, such as drones for surface water collection and systems equipped with wind and atmospheric CH_4 sensors, offer promising avenues for capturing these highly localized and transient CH_4 sources in future studies.

Data availability statement

The original contributions presented in the study are included in the article/Supplementary Material. Further inquiries can be directed to the corresponding author.

Author contributions

CH: Conceptualization, Investigation, Methodology, Supervision, Validation, Visualization, Writing – original draft, Writing – review & editing. BD: Formal analysis, Funding acquisition, Investigation, Methodology, Writing – original draft, Writing – review & editing. SL: Investigation, Methodology, Writing – original draft, Writing – review & editing. HC: Formal analysis, Methodology, Validation, Visualization, Writing – original draft, Writing – review & editing. RG: Methodology, Validation, Writing – original draft, Writing – review & editing. SJ: Conceptualization, Funding acquisition, Investigation, Writing – original draft, Writing – review & editing. JC: Conceptualization, Funding acquisition, Investigation, Methodology, Supervision, Validation, Writing – original draft, Writing – review & editing.

Funding

The author(s) declared that financial support was received for this work and/or its publication. We are grateful to the Swiss Polar Institute (SPI) which funded the GreenFjord project (SPI-FLAG-2021-002). C.H., S.L., H.C. and J.C. of the SENSE group at EPFL are supported by the Ferring Pharmaceuticals Margaretha Kamprad Chair in Environmental Sciences. The funder was not involved in the study design, collection, analysis, interpretation of data, the writing of this article, or the decision to submit it for publication. BD has received funding from GreenFeedBack (Greenhouse gas fluxes and earth system feedback) RIA funded by the European Union's HORIZON research and innovation program under grant agreement No 101056921. S.L.J acknowledges funding from the Swiss National Science Foundation (SNSF grant 2000021E_214835 - CARVICE).

Acknowledgments

We would like to thank the team of the *RV Forel* and *RV Sanna* for their assistance at sea, Andreas Vieli for fruitful exchange on EkaS dynamics, Maxi Castrillejo for help with CTD data management and discussions, Mihnea Surdu and Julia Schmale for wind speed measurements. We also thank A2 Photonic Sensors for their support and advice during the expeditions and with the following data treatment. Views and opinions expressed are, however, those of the authors only and do not necessarily reflect those of the European Union or CINEA. Neither the European Union nor the granting authority can be held responsible for them. BD is a research Associate at the F.R.S-FNRS.

Conflict of interest

The author(s) declared that this work was conducted in the absence of any commercial or financial relationships that could be construed as a potential conflict of interest.

Generative AI statement

The author(s) declared that generative AI was not used in the creation of this manuscript.

Any alternative text (alt text) provided alongside figures in this article has been generated by Frontiers with the support of artificial intelligence and reasonable efforts have been made to ensure accuracy, including review by the authors wherever possible. If you identify any issues, please contact us.

Publisher's note

Supplementary material

The Supplementary Material for this article can be found online at: https://www.frontiersin.org/articles/10.3389/fmars.2026.1797236/full#supplementary-material

References

Borges, A., Champenois, W., Gypens, N., Delille, B., and Harlay, J. (2016). Massive marine methane emissions from near-shore shallow coastal areas. *Sci. Rep.* 6, 27908. doi: 10.1038/srep27908

Christiansen, J. R., and Jørgensen, C. J. (2018). First observation of direct methane emission to the atmosphere from the subglacial domain of the Greenland ice sheet. *Sci. Rep.* 8, 16623. doi: 10.1038/s41598-018-35054-7

Colson, B. C., and Michel, A. P. M. (2025). Membrane equilibration for in situ dissolved gas instrumentation: a comparison of four approaches. *Front. Membr. Sci. Technol.* 4, 1488800. doi: 10.3389/frmst.2025.1488800

Damm, E., Erickson, Y., and Falck, E.. (2021). Waterside convection and stratification control methane spreading in supersaturated Arctic fjords (Spitsbergen). *Cont Shelf Res* 224, 104473. doi: 10.1016/j.csr.2021.104473

Damm, E., Rudels, B., Schauer, U., Mau, S., and Dieckmann, G. (2015). Methane excess in Arctic surface water – triggered by sea ice formation and melting. *Scientific Reports* 5, 16179. doi: 10.1038/srep16179

Damm, E., Schauer, U., Rudels, B., and Hass, C.. (2007). Excess of bottom-released methane in an Arctic shelf sea polynya in winter. *Cont Shelf Res* 27, 1692–1701. doi: 10.1016/j.csr.2007.02.003

Damm, E., Mackensen, A., Budéus, G., Faber, E., and Hanfland, C.. (2005). Pathways of methane in seawater: plume spreading in an Arctic shelf environment (SW-Spitsbergen). *Cont Shelf Res* 25, 1453–1472. doi: 10.1016/j.csr.2005.03.003

Dieser, M., Broemsen, E. L. J. E., Cameron, K. A., King, G. M., Achberger, A., Choquette, K., et al. (2014). Molecular and biogeochemical evidence for methane cycling beneath the western margin of the Greenland ice sheet. *ISME J.* 8, 2305–2316. doi: 10.1038/ismej.2014.59

Dolven, K. O., Vierinen, J., Grilli, R., Triest, J., and Ferré, B. (2022). Response time correction of slow-response sensor data by deconvolution of the growth-law equation. *Geosci. Instrum. Method. Data Syst.* 11, 293–306.

Ernst, L., Steinfeld, B., Barayeu, U., Klintzsch, T., Kurth, M., Grimm, D., et al. (2022). Methane formation driven by reactive oxygen species across all living organisms. *Nature* 603, 482–487. doi: 10.1038/s41586-022-04511-9

Fofonoff, N. P., and Millard, R. C. Jr.. (1983). Algorithms for computation of fundamental properties of seawater. *UNESCO technical papers in marine science*, No. 44. (Paris, France: UNESCO), 53. doi: 10.25607/OBP-1450

Gardner, A., Fahnestock, M., and Scambos, T.. (2022). MEaSUREs ITS_LIVE landsat image-pair glacier and ice sheet surface velocities, version 1. *NASA National Snow and Ice Data Center Distributed Active Archive Center*. doi: 10.5067/IMR9D3PEI28U

Gräff, D., Lipovsky, B. P., Vieli, A., Dachauer, A., Jackson, R. H., Farinotti, D., et al. (2025). Calving-driven fjord dynamics resolved by seafloor fibre sensing. *Nature* 644, 404–412. doi: 10.1038/s41586-025-09347-7

Grilli, R., Birot, D., Schumacher, M., Paris, J.-D., Blouzon, C., Donval, J. P., et al. (2021). Inter-comparison of the spatial distribution of methane in the water column from seafloor emissions at two sites in the western Black Sea using a multi-technique approach. *Front. Earth Sci.* 9, 626372. doi: 10.3389/feart.2021.626372

Grilli, R., DelSontro, T., Garnier, J., Jacob, F., and Némery, J. (2023). A novel high-resolution in situ tool for studying carbon biogeochemical processes in aquatic systems: the Lake Aiguebelette case study. *J. Geophys. Res. Biogeosci.* 128, e2022JG007200. doi: 10.1029/2022JG007200

Grilli, R., Triest, J., Chappellaz, J., Calzas, M., Desbois, T., Jansson, P., et al. (2018). SubOcean: Subsea dissolved methane measurements using an embedded laser spectrometer technology. *Environ. Sci. Technol.* 52, 10543–10551. doi: 10.1021/acs.est.7b06171

Hansen, K., Karlsson, N. B., How, P., Poulsen, E., Mortensen, J., and Rysgaard, S. (2025). Winter subglacial meltwater detected in a Greenland fjord. *Nat. Geosci.* 18, 219–225. doi: 10.31223/x5bx16

IPCC. (2021). Climate change 2021: the physical science basis. In: V. Masson-Delmotte, P. Zhai, A. Pirani, S. L. Connors, C. Péan, S. Berger, et al (eds.) *Contribution of Working Group I to the Sixth Assessment Report of the Intergovernmental Panel on Climate Change*. (Cambridge, UK: Cambridge University Press).

Mau, S., Blees, J., Helmke, E., Niemann, H., and Damm, E.. (2013). Vertical distribution of methane oxidation and methanotrophic response to elevated methane concentrations in stratified waters of the Arctic fjord Storfjorden (Svalbard, Norway). *Biogeosciences* 10, 6267–6278. doi: 10.5194/bg-10-6267-2013

Jähne, B., Heinz, G., and Dietrich, W. (1987). Measurement of the diffusion coefficients of sparingly soluble gases in water. *J. Geophys. Res. Oceans.* 92, 10767–10776.

Jansson, P., Triest, J., Grilli, R., Ferré, B., Silyakova, A., Mienert, J., et al. (2019). High-resolution underwater laser spectrometer sensing provides new insights into methane distribution at Arctic seepages site. *Ocean Sci.* 15, 1055–1069. doi: 10.5194/os-15-1055-2019

Jørgensen, C. J., Mønster, J., Fuglsang, K., and Christiansen, J. R. (2020). Continuous methane concentration measurements at the Greenland ice sheet–atmosphere interface using a low-cost, low-power metal oxide sensor system. *Atmos. Meas. Tech.* 13, 3319–3328. doi: 10.5194/amt-13-3319-2020

Kapit, J. A., Youngs, S., Pardis, W. A., Padilla, A. M., and Michel, A. P. M. (2024). An underwater methane sensor based on laser spectroscopy in a hollow core optical fiber. *ACS Sens.* 9, 5896–5905. doi: 10.1021/acssensors.4c01563

Kitidis, V., Upstill-Goddard, R. C., and Anderson, L. G.. (2010). Methane and nitrous oxide in surface water along the North-West Passage, Arctic Ocean. *Mar Chem* 121, 80–86. doi: 10.1016/j.marchem.2010.03.006

Kleber, G. E., Hodson, A. J., Magerl, L., Mannerfelt, E. S., Bradbury, H. J., Zhu, Y., et al. (2023). Groundwater springs formed during glacial retreat are a large source of methane in the high Arctic. *Nat. Geosci.* 16, 597–604. doi: 10.1038/s41561-023-01210-6

Kleber, G. E., Magerl, L., Turchyn, A. V., Schloemer, S., Trimmer, M., Zhu, Y., et al. (2025). Proglacial methane emissions driven by meltwater and groundwater flushing in a high-Arctic glacial catchment. *Biogeosciences* 22, 659–674. doi: 10.5194/bg-22-659-2025

Klintzsch, T., Geisinger, H., Wieland, A., Langer, G., Nehrke, G., Bizic, M., et al. (2023). Stable carbon isotope signature of methane released from phytoplankton. *Geophys. Res. Lett.* 50, e2023GL103317. doi: 10.1029/2023GL103317

Kudo, K., Yamada, K., Toyoda, S., Yoshida, N., Sasano, D., Kosugi, N., et al. (2018). Spatial distribution of dissolved methane and its source in the western Arctic Ocean. *J Oceanogr* 74, 305–317. doi: 10.1007/s10872-017-0460-y

Lamarche-Gagnon, G., Wadham, J. L., Sherwood Lollar, B., Arndt, S., Fietzek, P., Beaton, A. D., et al. (2019). Greenland melt drives continuous export of methane from the ice-sheet bed. *Nature* 565, 73–77. doi: 10.1038/s41586-018-0800-0

Lorenson, T. D., Greinert, J., Coffin, R. B., and Rehder, G.. (2016). Dissolved methane in the Beaufort Sea and the Arctic Ocean, 1992–2009: sources and atmospheric flux. *Limnol Oceanogr* 61, S300–S323. doi: 10.1002/lno.10457

Mankoff, K. D., Brice, N., Fettweis, X., Ahlstrøm, A. P., Colgan, W., Kondo, K., et al. (2020). Greenland liquid water discharge from 1958 through 2019. *Earth Syst. Sci. Data* 12, 2811–2841. doi: 10.5194/essd-12-2811-2020

Mankoff, K. D., and Tulaczyk, S. M.. (2017). The past, present, and future viscous heat dissipation available for Greenland subglacial conduit formation. *Cryosphere* 11, 303–317. doi: 10.5194/tc-11-303-2017

Manning, C. C. M., and Nicholson, D. P. (2022). dnicholson/gas_toolbox: MATLAB code for calculating gas fluxes. *Zenodo*. doi: 10.5281/zenodo.6126685

Mao, S.-H., Zhang, H.-H., Zhuang, G.-C., Li, X.-J., Liu, Q., Zhou, Z., et al (2024). Marine methane paradox: enigmatic production of methane in oxygenated waters. *Innovation Geosci.* 2, 100071. doi: 10.59717/j.xinn-geo.2024.100071

Mao, S. H., Zhang, H. H., Zhuang, G. C., Li, X.-J., Liu, O., et al. (2022). Aerobic oxidation of methane significantly reduces global diffusive methane emissions from shallow marine waters. *Nat. Commun.* 13, 7309. doi: 10.1038/s41467-022-35082-y

Meire, L., Mortensen, J., Meire, P., Juul-Pedersen, T., Sejr, M. K., Rysgaard, S., et al. (2017). Marine-terminating glaciers sustain high productivity in Greenland fjords. *Glob. Change Biol.* 23, 5344–5357. doi: 10.1111/gcb.13801

Morville, J., Romanini, D., and Kerstel, E. (2014). "Cavity enhanced absorption spectroscopy with optical feedback," in *Cavity-Enhanced Spectroscopy and Sensing*. Eds. G. Gagliardi and H.-P. Loock (Springer, Berlin Heidelberg), 163–209.

Nightingale, P. D., Malin, G., Law, C. S., Watson, A. J., Liss, P. S., Liddicoat, M. I., et al. (2000). In situ evaluation of air-sea gas exchange parameterizations using novel conservative and volatile tracers. *Global Biogeochem Cycles* 14, 373–387. doi: 10.1029/1999GB900091

Overeem, I., Hudson, B. D., Syvitski, J. P. M., Mikkelsen, A. B., Hasholt, B., van den Broeke, M. R., et al. (2017). Substantial export of suspended sediment to the global oceans from glacial erosion in Greenland. *Nat. Geosci.* 10, 859–863. doi: 10.1038/ngeo3046

Perez-Coronel, E., and Beman, M. J. (2022). Multiple sources of aerobic methane production in aquatic ecosystems include bacterial photosynthesis. *Nat. Commun.* 13, 6454. doi: 10.1038/s41467-022-34105-y

Ploug, H., Kühl, M., Buchholz-Cleven, B., and Jørgensen, B. B.. (1997). Anoxic aggregates – an ephemeral phenomenon in the pelagic environment? *Aquat Microb Ecol* 13, 285–294. doi: 10.3354/ame013285

Poinart, K., Box, J. E., Mote, T. L., Loomis, B. D., Smith, B. E., Medley, B. C., et al. (2024). Greenland ice sheet. In: *NOAA Arctic report card 2024*. doi: 10.25923/njxd-b82

Portnov, A., Vadakkepuliyambatta, S., Mienert, J., and Hubbard, A. (2016). Ice-sheet-driven methane storage and release in the Arctic. *Nat. Commun.* 7, 10314. doi: 10.1038/ncomms10314

Reeburgh, W. S.. (2007). Oceanic methane biogeochemistry. *Chem Rev* 107, 486–513. doi: 10.1021/cr050362v

Repeta, D., Ferrón, S., Sosa, O., Johnson, C. G., Repeta, L. D., Acker, M., et al. (2016). Marine methane paradox explained by bacterial degradation of dissolved organic matter. *Nat. Geosci.* 9, 884–887. doi: 10.1038/ngeo2837

Rhee, T. S., Kettle, A. J., and Andreae, M. O. (2009). Methane and nitrous oxide emissions from the ocean: a reassessment using basin-wide observations in the Atlantic. *J. Geophys. Res.* 114, D12304. doi: 10.1029/2008JD011662

Rocher-Ros, G., Stanley, E. H., Loken, L. C., Casson, L. C., Raymond, P. A., Liu, S., et al. (2023). Global methane emissions from rivers and streams. *Nature* 621, 530–535. doi: 10.1038/s41586-023-06344-6

Rodes, N., Betlem, P., Senger, K., Römer, M., Hodson, A., Liira, M., et al. (2023). Active gas seepage in western Spitsbergen fjords, Svalbard archipelago: spatial extent and geological controls. *Front. Earth Sci.* 11, 1173477. doi: 10.3389/feart.2023.1173477

Rosentreter, J. A., Borges, A. V., Deemer, B. R., Holgerson, M. A., Liu, S., Song, C., et al. (2021). Half of global methane emissions come from highly variable aquatic ecosystem sources. *Nat. Geosci.* 14, 225–230. doi: 10.1038/s41561-021-00715-2

Straneo, F., and Cenedese, C. (2015). The dynamics of Greenland's glacial fjords and their role in climate. *Annu. Rev. Mar. Sci.* 7, 89–112. doi: 10.1146/annurev-marine-010213-135133

Strock, K. E., Krewson, R., Hayes, N. M., and Deemer, B. R.. (2024). Oxidation is a potentially significant methane sink in land-terminating glacial runoff. *Sci Rep* 14, 23389. doi: 10.1038/s41598-024-73041-3

Szymczycha, B., Diak, M., Hong, W.-L., Böttcher, M. E., Lepland, A., Makuch, P., et al. (2025). Submarine groundwater discharge and gas hydrate dissociation fuel organic matter formation in Arctic fjord sediments. *Mar. Chem.* 273, 104570. doi: 10.1016/j.marchem.2025.104570

Triest, J., Chappellaz, J., and Grilli, R. (2017). "System forfast and in-situ sampling of dissolved gases in the ocean," in *Patent 08276-01* (CNRS, Grenoble, France).

Upstill-Goddard, R. C., Rees, A. P., and Owens, N. J. P. (1996). Simultaneous high-precision measurements of methane and nitrous oxide in water and seawater by single phase equilibration gas chromatography. *Deep Sea Res. I.* 43, 1669–1682. doi: 10.1016/s0967-0637(96)00074-x

Verdugo, J., Damm, E., Schaffer, J., Bauch, D., Meyer, H., and Kaiser, J.. (2022). Impacts of glacier and sea ice melt on methane pathways on the Northeast Greenland shelf. *Cont Shelf Res* 243, 104752. doi: 10.1016/j.csr.2022.104752

Vinogradova, E., Damm, E., Pnyushkov, A. V., Krumpen, T., and Ivanov, V. V.. (2022). Shelf-sourced methane in surface seawater at the Eurasian continental slope (Arctic Ocean). *Front Environ Sci* 10, 811375. doi: 10.3389/fenvs.2022.811375

Vogt, J., Risk, D., Bourlon, E., Azetsu-Scott, K., Edinger, E. N., Sherwood, O. A., et al. (2023). Sea-air methane flux estimates derived from marine surface observations and instantaneous atmospheric measurements in the northern Labrador Sea and Baffin Bay. *Biogeosciences* 20, 1773–1787. doi: 10.5194/bg-20-1773-2023

Wanninkhof, R. (2014). Relationship between wind speed and gas exchange over the ocean revisited. *Limnol. Oceanogr. Methods* 12, 351–362. doi: 10.4319/lom.2014.12.351

Weiss, R. F. (1981). Determinations of carbon dioxide and methane by dual catalyst flame ionization chromatography and nitrous oxide by electron capture chromatography. *J. Chromatographic Sci.* 19, 611–616. doi: 10.1093/chromsci/19.12.611

Wiesenberg, D. A., and Guinasso, N. L. (1979). Equilibrium solubilities of methane, carbon monoxide, and hydrogen in water and sea water. *J. Chem. Eng. Data* 24, 356–360.

Wood, M., Carroll, D., Fenty, I., Bertin, C., Darby, B., Dutkiewicz, S., et al. (2025). Increased melt from Greenland's most active glacier fuels enhanced coastal productivity. *Commun. Earth Environ.* 6, 626. doi: 10.1038/s43247-025-02599-1

Ye, J., Zhuang, M., Hong, M., Zhang, D., Ren, G., Hu, A., et al. (2024). Methanogenesis in the presence of oxygenic photosynthetic bacteria may contribute to global methane cycle. *Nat. Commun.* 15, 5682. doi: 10.1038/s41467-024-50108-3

Ye, W., Li, Y., Wen, J., Zhang, J., Shakhova, N., Liu, J., et al. (2023). Enhanced transport of dissolved methane from the Chukchi Sea to the central Arctic. *Global Biogeochem Cycles* 37, e2022GB007368. doi: 10.1029/2022GB007368